Highly efficient and selective carbon-doped BN photocatalyst derived from a homogeneous precursor reconfiguration

Qiong Lu [1, 2], Jing An [3], Yandong Duan [3]*, Qingzhi Luo [3], Yunyun Shang [3], Qiunan Liu [4], Yongfu Tang [4], Jianyu Huang [3], Chengchun Tang [1, 2]*, Rong Yin [3] and Desong Wang [1, 3, 4]*

[1] School of Materials Science and Engineering, Hebei University of Technology, Tianjin 300130, People's Republic of China; qiong253@163.com

[2] Hebei Key Laboratory of Boron Nitride Micro and Nano Materials, Hebei University of Technology, Tianjin 300130, People's Republic of China

[3] Hebei Key Lab of Photoelectric Control on Surface and Interface, School of Sciences, Hebei University of Science and Technology, Shijiazhuang 050018, People's Republic of China; anjinghebust@163.com; lqz2004-1@163.com; 978890711@qq.com; yinrong6868@163.com

[4] Applying Chemistry Key Laboratory of Hebei Province, State Key Laboratory of Metastable Materials Science and Technology, Yanshan University, Qinhuangdao, 066004, People's Republic of China; 13731790498@163.com; tangyongfu@ysu.edu.cn; jyhuang8@hotmail.com

* Correspondence: dswang06@126.com; tangcc@hebut.edu.cn; ydduan@iccas.ac.cn

Table S1 Crystal data and structure refinement for M·2B

Empirical formula	$C_3H_{12}B_2N_6O_6$
Formula weight	249.81
Temperature	190(2) K
Wavelength	1.34139 Å
Crystal system	Monoclinic
Space group	$P2_1/c$
Unit cell dimensions	a = 3.5559(5) Å □α= 90°
	b = 20.021(3) Å □β= 92.648(7)°
	c = 14.0894(19) Å □γ= 90°
Volume	1002.0(2) $Å^3$
Z	4
Density (calculated)	1.656 g/cm^3
Absorption coefficient	0.819 mm^{-1}
F(000)	520
Crystal size	0.120 × 0.110 × 0.080 mm^3
Theta range for data collection	3.339 to 54.080°
Index ranges	-4<=h<=4, -24<=k<=24, -16<=l<=16
Reflections collected	18890
Independent reflections	1848 [R(int) = 0.0845]
Completeness to theta = 53.594°	100.0 %
Refinement method	Full-matrix least-squares on F^2
Data / restraints / parameters	1848 / 0 / 160
Goodness-of-fit on F^2	1.076
Final R indices [I>2sigma(I)]	R1 = 0.0524, wR2 = 0.1464
R indices (all data)	R1 = 0.0688, wR2 = 0.1593
Extinction coefficient	n/a
Largest diff. peak and hole	0.229 and -0.332 $e.Å^{-3}$

Single crystal structure determination by X-ray diffraction was performed with a Bruker APEX-II CCD diffractometer equipped with a normal focus, 2.4 kW sealed tube X-ray source (Ga Kα radiation, λ = 1.34139 Å) operating at 50 kV and 40 mA. A hemisphere of intensity data was collected at 190 K in the 2θ range 3.339 to 54.080°. The structure was solved with the ShelXT [Sheldrick, 2018] structure solution program using Intrinsic Phasing and refined with the ShelXL [Sheldrick, 2018] refinement package using Least Squares minimisation.

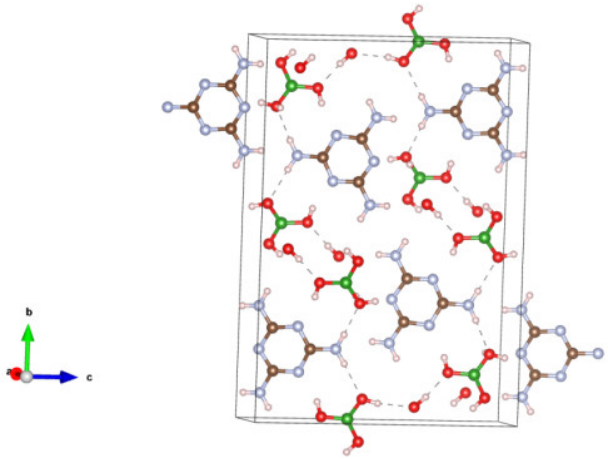

Figure S1. Arrangements of melamine and boric acid molecules in the crystal of M·2B, view along crystallographic an axis, dashed lines represent intermolecular hydrogen bonds. When viewed along the a-axis, melamine and boric acid molecules are connected together by hydrogen bonds to form a layer like structure in the bc-plane [1, 2]. The single crystal structure of M·2B shows the asymmetric unit and the stacking arrangement of a three-dimensional hydrogen-bonded supramolecular networks involving O–H···O, N–H···O and O–H···N hydrogen bonds.

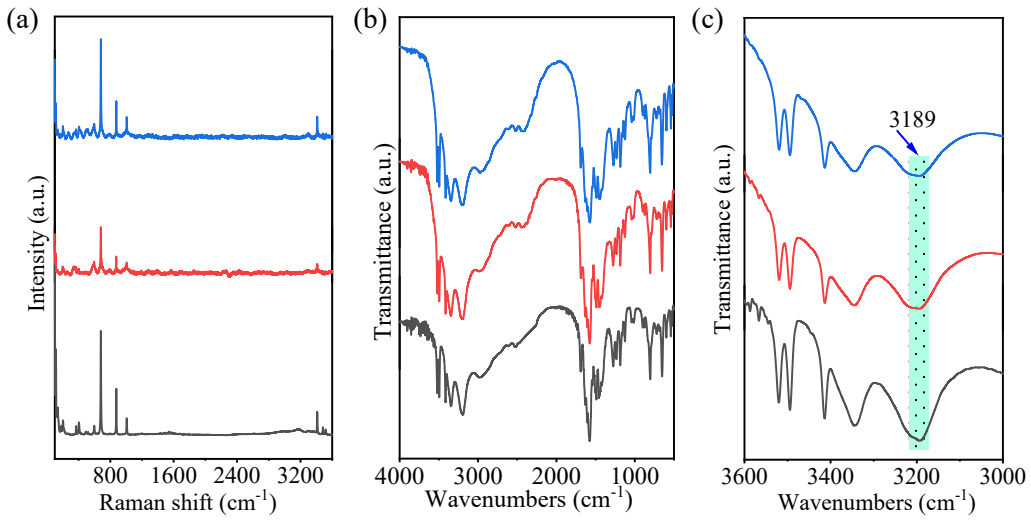

Figure S2. Raman (a) and FTIR spectra of M·2B (black line), P1 (red line) and P2 (blue line): (b) in the 500~4000 cm^{-1} region; (c) in the 3000~3600 cm^{-1} region.

Table S2 Spectral data (cm^{-1}) and band assignments of M·2B, P1 and P2

Raman (cm^{-1})			IR (cm^{-1})			Assignments
M·2B	P1	P2	M·2B	P1	P2	
3518_s, 3483_s, 3410_{vs}	3518_{vw}, 3483_{vw}, 3410_m	3518_m, 3483_m, 3410_{vs}	3520_s, 3493_s, 3413_s	3520_s, 3493_s 3413_s	3520_s, 3493_s, 3413_s	free N-H bonds
3362_w, 3298_w	3298_{vwbr}	3299_m	3345_s	3345_{sbr}	3345_{sbr}	the stretching modes of the hydrogenbonded N-H bonds
3187_m			3189_m	3189_{wbr}	3189_{wbr}	O-H stretching mode
1675_{vw}	1695_{vwbr}	1647_{vwbr}	1690_{vvwbr}, 1669_{vw}	1689_{vvwbr}, 1670_{vw}	$1690_{vwbr,}$ 1669_{vw}	NH_2 bending
				1685_{vw}, 1676_{vw}, 1663_{vw}		hemiacetal group
1569_w, 1535_w, 1512_{vw}	1569_w		1576_{wbr}, 1540_{vw}, 1506_{vw}	1575_{wbr}, 1540_{vvw}, 1506_{vvw}	1574_{wbr}, 1538_{vvw}, 1504_{vvw}	NH_2 bending and Ring distortion
1488_{vw}	1493_{vw}	1482vw	1489_w	1490_w	1489_w	Symmetric bending of the C atoms of triazine ring
			1456			
1200_{vw}	1275_{vw}					BOH bend
1166_{vw}	1177_{vwbr}	1166_{vwbr}	1185_m, 1158_w, 1125_m	1185_m, 1158_w, 1125_m	1185_m,1158_w, 1125_m	Melamine bands corresponding to 1195 and 1175 cm^{-1}
1138_w			1140_w	1140_{vw}	1140_w	BOH bend
1008_w	1008_{vw}	1008_w	1112w	1115vw	1112w	Ring breathing mode of N atoms of Symmetric melamine
876_m	876_m	876_m	873_m	873_m	873_m	νB-O
681_s	681_s	681_s	652_{vs}	652_{vs}	652_{vs}	Ring breathing mode of C atoms of melamine
597_w, 520_{vw}	593_{wbr}, 520_{vvw}	597_{wbr}, 520_{vwbr}	598_s, 538_s	598_w, 538_w	598_m, 538_m	OBO bending
404_w, 369_w	404_w, 369_w	404_w, 369_w				CN rocking
204_w	200_{wbr}	204_{vw}				OH twist
181_w	181_{vw}	181_{vw}				
138_w	138_{vw}	138_{vw}				External modes of melamine
114_w	114_{vw}	114_{vw}				Totally symmetric lattice vibration

v, very; w, weak; m, medium; s strong; br, broad

Table S3. Chemical Shifts of ^{13}C of glucose, P1 and P2

Sample	**C(1)**	**C(2)**	**C(3)**	**C(4)**	**C(5)**	**C(6)**
$C_6H_{12}O_6$	111.11	87.52	99.64	78.43	91.70	68.95
P1	108.66	85.25	99.64	75.07	92.97	69.44
P2	110.96	87.52	99.95	72.66	92.85	67.76

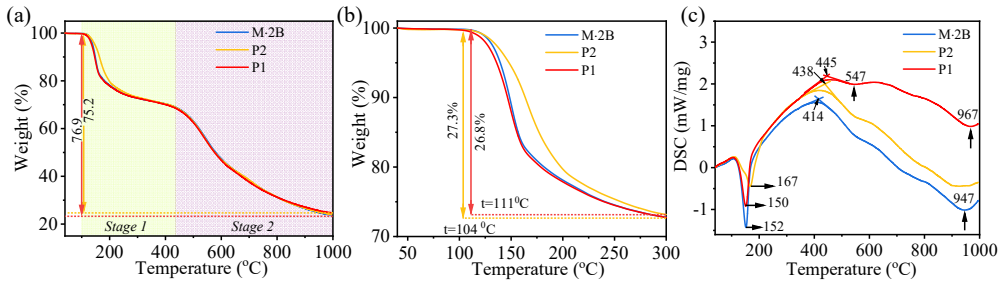

Figure S3. TGA thermograms of M·2B, P1 and P2 samples: (a) from 40 to 1000 °C in N_2; (b) from 40 to 300 °C in N_2 and (c) DSC curves of M·2B, P1 and P2 samples from 40 °C to 1000 °C in N_2.

The whole pyrolysis procedure can be divided into two weight-loss stages (Figure S3a). In the first stage (100 ~ 300 °C), there is a sharp endothermic peak from 150 °C to 167 °C for three different precursors due to intense weight loss corresponding to the release of H_2O (Figure S3c). The temperature of endothermic peaks of P1 (150 °C) and P2 (167 °C) is different from that of M·2B. The weight loss of P1 is 0.5 wt.% more than that of M·2B (Figure S3b). It can be clearly observed that the weight loss of P1 (1.7 wt.%) is less than that of P2 (Figure S3b), indicating that glucose is more evenly dispersed in P1 and more carbon element remained in p-BCN-1 structure by thermal decomposition of P1 comparing with P2. The temperatures of exothermic peaks of P1 (445 °C) and P2 (438 °C) are higher from that of M·2B (413 °C) as displayed in Figure S3c, and an endothermic peak at 547 °C was only detected in P1.

According to the TG-DSC analysis, it is reasonably predicted to obtain more effective p-BCN by calcining the precursors slowly overheating from 100 °C to 300 °C. Therefore, the precursor was heated in an N_2 atmosphere at 300 °C for 2 h with a ramp rate of 2 °C·min^{-1} and enough time under static heating at 300 °C, which ensures the

reactions to proceed completely. During the second stage, the gravimetric curve is gradually downward from 430 °C to 1000 °C, attributed to the release of NH_3 occurring in the range of 430~600 °C due to the condensation of melamine, and the release of CO_2 happening at ca. 450 °C and reach to the substantial release in the range of 500~700 °C, the release of HCN and CO_2 occurring in the range of 700~1000 °C [3]. Those results exhibit in the form of weight loosening.

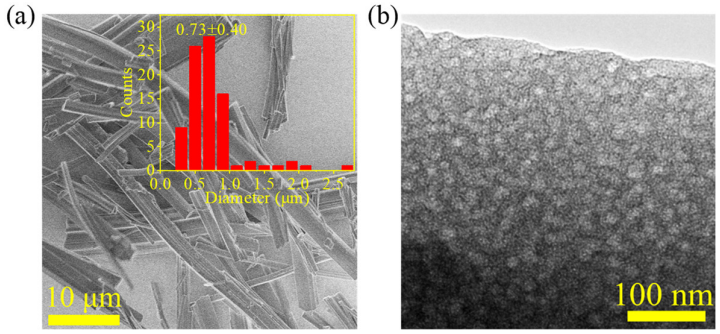

Figure S4. (a) The SEM image of p-BCN-1, inset: the diameter distribution histogram. (b) The HRTEM image of p-BCN-1

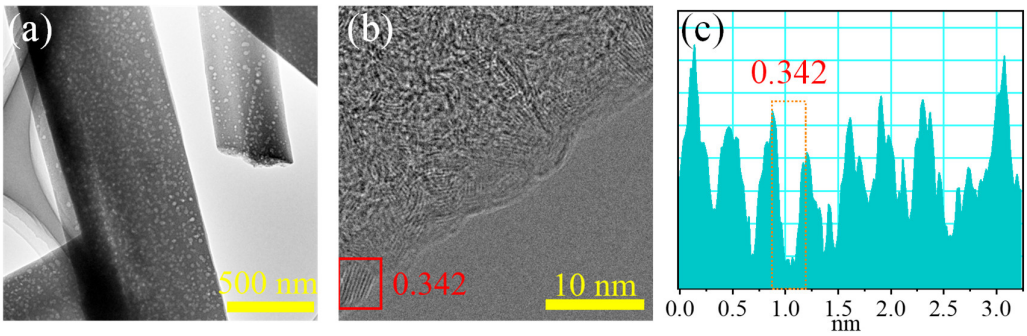

Figure S5. Morphologies of the p-BN: (a) TEM (scale bar: 500 nm); (b) HRTEM (scale bar: 10 nm). (c) Measured the layer distance of the red rectangle of (b), the interspacing is 0.342 nm.

Table S4. Physical and textural properties of p-BN, p-BCN-1 and p-BCN-2

Sample	S_{BET}[a] (m^2/g)	V_{pore}[b] (cm^3/g)	D_{pore}[c] (nm)
p-BN	1018	0.651	2.5
p-BCN-1	918	0.605	2.7
p-BCN-2	730	0.512	2.8

[a] Specific surface area by BET method. [b]Pore volume at p/p_0=0.99.

[c] BJH desorption average pore width.

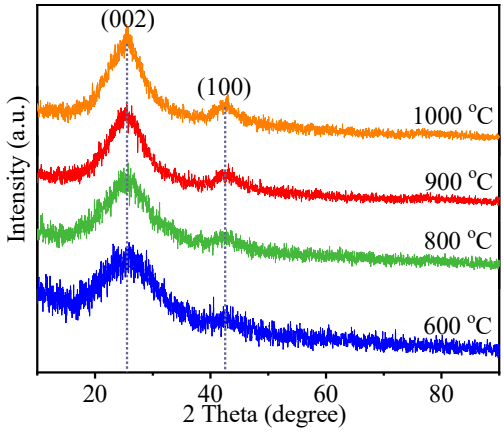

Figure S6. Powder XRD patterns of calcined product p-BCN-1 of the P1 at different temperatures.

The sample calcined at 600 °C only shows a broadened and weak XRD diffraction peak at 2θ = 25.7° corresponded to (002) plane, exhibiting the poor crystallinity of h-BN. When the calcination temperature rises to 800℃, a new peak appears at 2θ = 42.7°, which belongs to the (100) plane. As the calcination temperature rising to 900 °C and 1000 °C, two similarly diffraction peaks appear, with slight band sharpening and an increase of the band intensity of (002) and (100) planes, accompanied by a slight shift of the peak to higher angles (ca. 2θ = 25.6~25.7°) than that of p-BN, which are between the 2θ value of graphene and h-BN [4]. The results confirm that higher crystallinity directly correlates with higher calcination temperature.

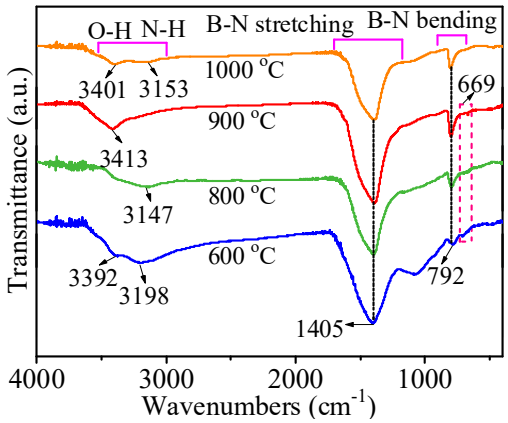

Figure S7. FTIR spectra of calcined product p-BCN-1 of the P1 at different temperatures.

In the FTIR spectra, it is found that the sample calcined at 600 °C has a broadened peak and a very weak peak at 1405 cm^{-1} and 792 cm^{-1}, assigned to the in-plane stretching bands of sp^2-bonded B−N and the out-of-plane B−N bending bands of sp^2-bonded B–N–B, respectively, as well as several weak peaks between the two peaks, meaning intrinsic structure of h-BN is formed incompletely. However, as calcination temperatures increased from 800 °C to 1000 °C, a slight band sharpening and an increase of the band intensity of peaks at 1405 cm^{-1} and 792 cm^{-1} of intrinsic structure of h-BN were observed, inferring the intrinsic structure of h-BN is formed gradually. The results are consistent with the XRD analysis. The broad bands ranging from 3100 cm^{-1} to 3450 cm^{-1} can be assigned to B−OH and B−NH_2.

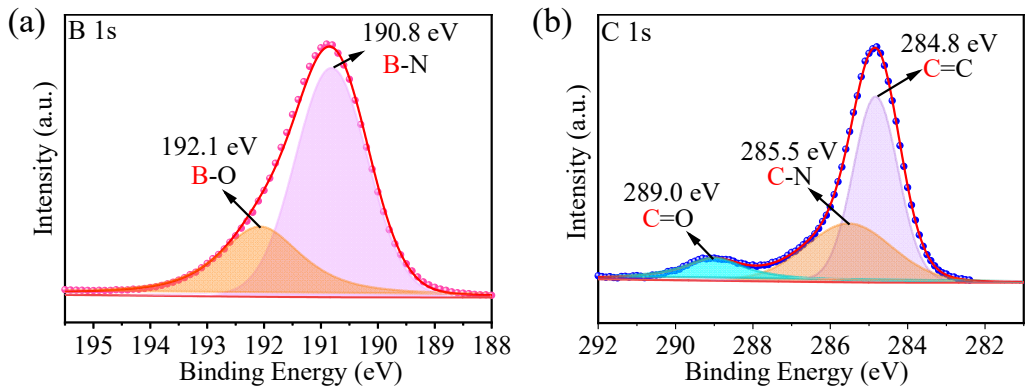

Figure S8. XPS high-resolved spectra of p-BN, (a) B 1s and (b) C 1s.

Table S5. The peak position and relative atomic percentage of various functional groups in p-BN, p-BCN-1 and p-BCN-2 samples

Sample	B						N				C								O					
	B-C		B-N		B-O		N-B		N-C		B-C		C=C		C-N		C=O		B-O		C=O		C-O-C	
	eV	%	eV	%	eV	%	eV	%	eV	%	eV	%	eV	%	eV	%	eV	%	eV	%	eV	%	eV	%
p-BN	-	-	190.8	67.63	192.1	32.36	398.4	58.59	398.8	41.41	-	-	284.8	54.36	285.5	32.51	289.0	13.12	531.7	22.42	532.6	42.53	533.3	35.05
p-BCN-1	189.9	5.94	190.8	59.88	192.1	34.17	398.3	65.56	399.0	34.44	284.1	21.25	284.8	42.38	286.0	21.44	289.0	14.93	531.7	30.71	532.6	44.18	533.5	25.11
p-BCN-2	189.9	2.72	190.8	61.73	192.1	35.55	398.4	67.54	398.8	32.46	284.1	4.33	284.8	56.77	285.7	30.47	289.0	8.42	531.7	21.23	532.6	39.85	533.3	38.91

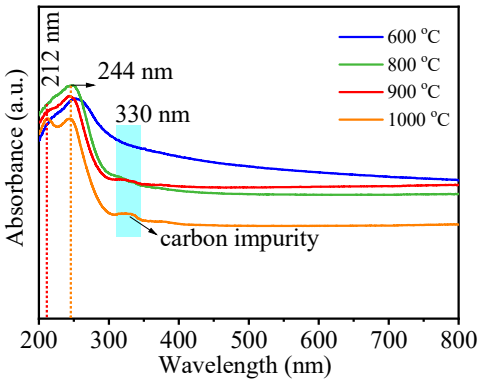

Figure S9. UV-vis diffuse reflectance spectra of calcined product p-BCN-1 of the P1 at different temperatures.

Only an absorption peak at around 244 nm is detected at 600 ºC and 800 ºC. With the increase of calcination temperature, three absorption peaks are obtained at about 212, 244 and 330 nm at 900 ºC and 1000 ºC, respectively.

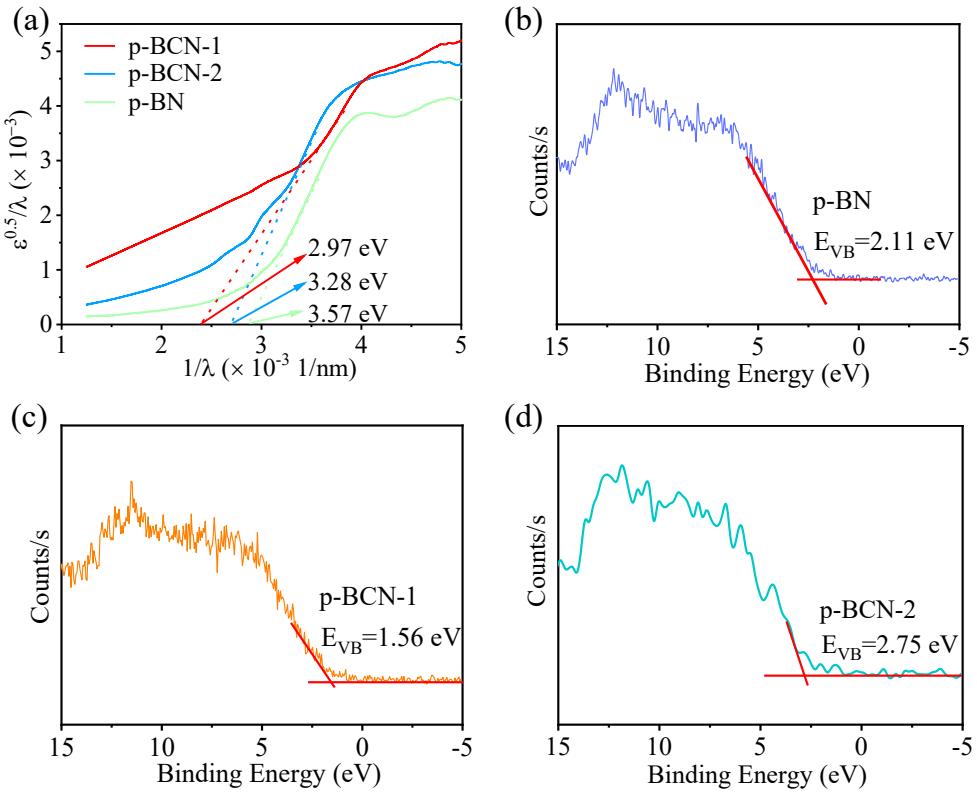

Figure S10. (a) Plots of $\varepsilon^{0.5}/\lambda$ versus $1/\lambda$ based on the optical absorption data from p-BN, p-BCN-1 and p-BCN-2 samples, respectively. VB-XPS spectra of (b) p-BN, (c) p-BCN-1 and (d) p-BCN-2.

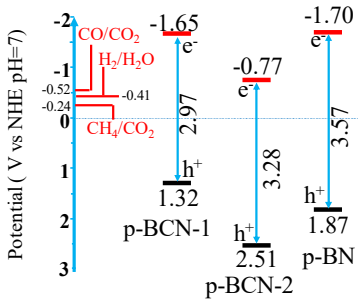

Figure S11. Schematic illustration of the band structures of p-BN, p-BCN-1 and p-BCN-2 samples, the redox potential of CO_2 at pH=7, with respect to NHE.

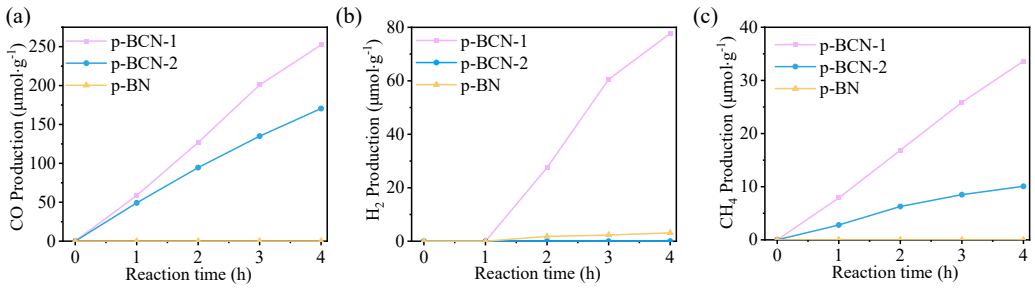

Figure S12. Photocatalytic activities over the p-BN, p-BCN-1 and p-BCN-2 samples: (a) CO production, (b) H_2 production and (c) CH_4 production.

1. Experimental section

1.1 Apparatus and characterization

X-ray diffraction (XRD) patterns of the as-obtained samples were characterized on an X-ray diffractometer (D/MAX-2500, Rigaku, Japan), operating at 40 kV and 150 mA using Cu K_α radiation (λ=0.15406 nm) with a scanning angle 2θ of 5~100°. Fourier transform infrared spectra (FTIR) of the samples were performed on a FTIR spectrometer (Prestige-21, Shimadzu, Japan, 400~4000 cm^{-1}) using KBr as the reference sample. Raman spectra were acquired by a Raman microspectrometer (LabRAM HR Evolution, HORIBA J Y, France, 100~4000 cm^{-1}) at a resolution of 0.6 cm^{-1} using a 532 nm laser excitation. Element analysis (Elementar vario EL cube, Thermal Conductivity Detector) was used to measure the precise carbon (C), nitrogen (N) and hydrogen (H) in the composites by CHN mode. The element chemical state of the samples was investigated on an X-ray photoelectron spectrometer (Thermo Scientific *K*-Alpha$^+$, Thermofisher, US) using Al K_α radiation (hv =1486.6 eV). ^{11}B, ^{13}C and ^{1}H solid state nuclear magnetic resonance (NMR) spectra of the materials were recorded on an Agilent 600M equipped with a Bruker DSX-300 spectrometer accompanied by high power decoupling using a Bruker 4mm magic angle spinning (MAS) probe head. The spinning rate was 8 kHz, and the delay between the two pulses was varied between 1 and 30 s to ensure complete relaxation of the ^{31}P nuclei. The chemical shifts were given relative to external TMS for the proton and carbon and BF_3OEt_2 for boron. Morphology of the samples was obtained by scanning electron microscope (SEM) (S-4800, Hitachi, Japan, 10.0 kV) and a bright field and the high

resolution transmission electron microscope (FEI Titan^{TM} ETEM G2) images were collected at 300 kV accelerating voltage. Electron energy loss spectroscopy (EELS) analysis was performed to determine the distribution of carbon. UV-vis diffuse reflectance spectroscopy (UV-vis DRS) was measured with $BaSO_4$ as the background on a Scan UV-vis system (SHIMADZU-2550, Shimadzu, Japan, 200~800 nm) combined with an integrating sphere attachment. Thermogravimetric analysis (TG) and differential scanning calorimetry (DSC) of the sample were performed on a TG/DSC analyzer (NETZSCH STA 449F5, Germany) at a rate of 5 °C/min under N_2 flow. Brunauer-Emmett-Teller (BET) surface areas were examined by N_2 adsorption-desorption isotherms instrument (Tristar II 3020 2.00, Micromeritics, US, 77 K). The pore-size distribution curve and porosity properties were determined by the Barret, Joyner, and Halenda (BJH) method. Electrochemical impedance spectra (EIS) and photocurrent were detected on a CHI 660E electrochemical system (CH Instruments, China) under xenon light irradiation. A three-electrode quartz cell was used for measurement with Pt as the counter electrode, Ag/AgCl as reference electrode, the thin film of p-BCN or p-BN on indium−tin oxide (ITO) glass as the working electrode, and 0.2 mol L^{-1} Na_2SO_4 aqueous solutions as the electrolyte, respectively. The electron paramagnetic resonance (EPR) of samples was measured using Bruker EMX PLUS. The resonance frequency is 9.82 GHz.

1.2 Photocatalytic performance test for CO_2 reduction

The photocatalytic reduction of CO_2 was conducted in a 150 mL gas-closed quartz glass reactor on an online photoreaction system (Beijing Perfectlight, LabSolarIIIAG).

In a typical photocatalytic CO_2 reduction reaction, 50 mg of sample was evenly dispersed in a quartz Petri dish with an irradiation area of 28 cm^2. Then, the other dish with 3 mL of deionized water was put in the reactor and the quartz Petri dish was put on it. The reaction system was continuously purged with high purity CO_2 gas (1 atm) in the dark for 30 min to achieve CO_2 adsorption-desorption equilibrium before light irradiation. The reactor was irradiated by a 300 W Xe lamp (PLS-SXE300) with a focus intensity of 0.61 W/cm^2 to simulate the sunlight. The photocatalytic test was performed at room temperature controlled by a low-temperature thermostat bath system. Every 2 h, 1 mL of the generated gaseous products (CO, H_2 and CH_4) were collected and quantified by using GC9700 gas chromatography (Fuli instruments, China) equipped with Thermal Conductivity Detector (TCD) and Flame Ionization Detector (FID) using N_2 as the carrier gas.

The reduction selectivity of CO, CH_4 and H_2 can be described as [5]:

$$S_{CO} = \frac{2R_{CO}}{2R_{CO} + 8R_{CH_4} + 2R_{H_2}} \times 100\%$$

$$S_{CH_4} = \frac{8R_{CH_4}}{2R_{CO} + 8R_{CH_4} + 2R_{H_2}} \times 100\%$$

$$S_{H_2} = \frac{2R_{H_2}}{2R_{CO} + 8R_{CH_4} + 2R_{H_2}} \times 100\%$$

Herein, *R* represents the productive rates of products.

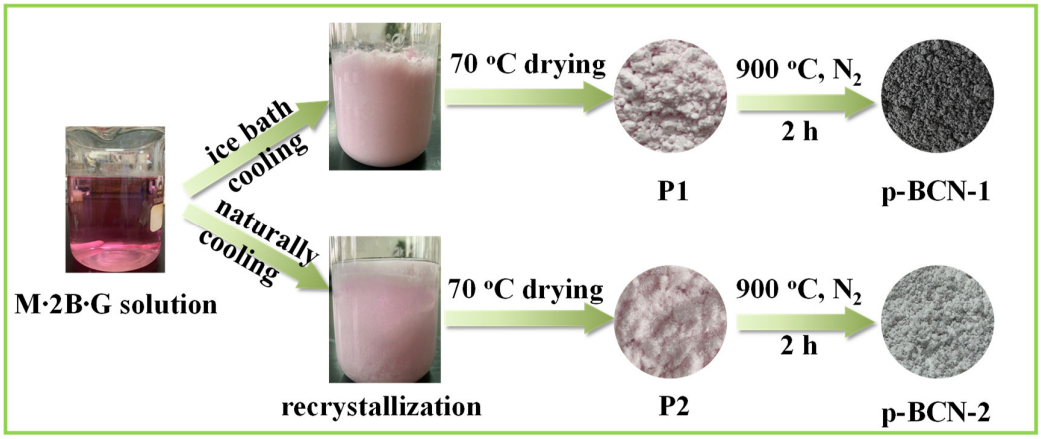

Figure S13. Photographic synthesis of the p-BCN samples by two different cooling modes.

M·2B·G solution is slightly acidic at pH 5.5, the solution appears pink due to the formation of hydrogen bonds between the free N−H bonds of melamine and the O−H bonds of glucose under acidic conditions.

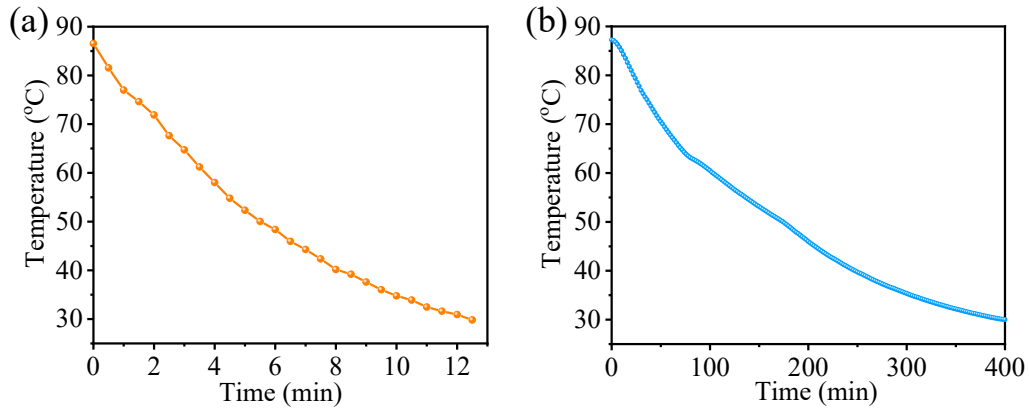

Figure S14. Cooling curves of (a) P1 and (b) P2. When the temperature of M·2B·G aqueous solution dropped from 90 °C to 30 °C, it took 12 min by ice bath rapid cooling (The temperature of the ice water bath was 4 °C), while it took 400 min by natural cooling.

References

1. Roy, A.; Choudhury, A.; Rao, C.N.R. Supramolecular hydrogen-bonded structure of a 1:2 adduct of melamine with boric acid. *J. Mol. Struct.* **2002**, 613, 61-66.
2. Wang, K.; Duan, D.; Wang, R.; Lin, A.; Cui, Q.; Liu, B.; Cui, T.; Zou, B.; Zhang, X.; Hu, J.; Zou, G.; Mao, H.-k. Stability of hydrogen-bonded supramolecular architecture under high pressure conditions: Pressure-induced amorphization in melamine-boric Acid adduct. *Langmuir* **2009**, 25, 4787-4791.
3. Wu, C.; Wang, B.; Wu, N.; Han, C.; Zhang, X.; Shen, S.; Tian, Q.; Qin, C.; Li, P.; Wang, Y. Molecular-scale understanding on the structure evolution from melamine diborate supramolecule to boron nitride fibers. *Ceram. Int.* **2020**, 46, 1083-1090.
4. Wang, J.; Hao, J.; Liu, D.; Qin, S.; Portehault, D.; Li, Y.; Chen, Y.; Lei, W. Porous boron carbon nitride nanosheets as efficient metal-free catalysts for the oxygen reduction reaction in both alkaline and acidic solutions. *ACS Energy Lett.* **2017**, 2, 306-312.
5. Fu, J.; Jiang, K.; Qiu, X.; Yu, J.; Liu, M. Product selectivity of photocatalytic CO_2 reduction reactions, *Mater. Today*, **2020**, 32, 222-243.